Supplemental Information on Efficient THz sensing

Serhii Shafraniuk

Tegri LLC, 558 Michigan, Evanston, 60202, IL, USA.

Corresponding author(s). E-mail(s): serhii.sh@gmail.com;

Keywords: entangled,graphene, laser, terahertz, coherent photon

1 Nonequilibrium dynamics of GEP in terms of the Maxwell–Bloch equations

The key element of the single-photon laser serving as the entangled photon generator is the graphene quantum dot depicted in Fig. 1.

When considering the graphene quantum dot laser, we focus mainly on the carrier capture and relaxation dynamics. For the sake of simplicity, we do not discuss multi-mode behavior, such as mode hopping and competition, and thus assume a single-mode microcavity laser. Besides, we disregard all transverse field effects. In this limit, the laser field equation may be written as

$$E\left(z,t\right)=\frac{1}{2}\mathcal{E}\left(t\right)u\left(z\right)\exp\left(-i\omega t\right)+c.c., \tag{1}$$

where z is the position along the laser axis, t is the time, $\mathcal{E}\left(t\right)$ is a slowly varying complex electric field amplitude, ω is the laser frequency, and $u\left(z\right)$ is the passive resonator eigenfunction. The Maxwell–Bloch equations (4)–(6) describe the coupled laser field and gain medium. The system includes the reduced laser field wave equation complemented by the semiconductor Bloch equations for the active region [1]. In terms of the Maxwell–Bloch equations in assumption of slowly varying amplitude and phase we have

$$\frac{d\mathcal{E}\left(t\right)}{dt}=-\gamma_{c}\mathcal{E}\left(t\right)+\frac{i\omega\Gamma}{\varepsilon_{b}}P\left(t\right), \tag{2}$$

where γ_{c} is the cavity linewidth, ε_{b} is the background permittivity, Γ is the optical mode confinement factor. The slowly varying complex polarization amplitude, $P\left(t\right)$,

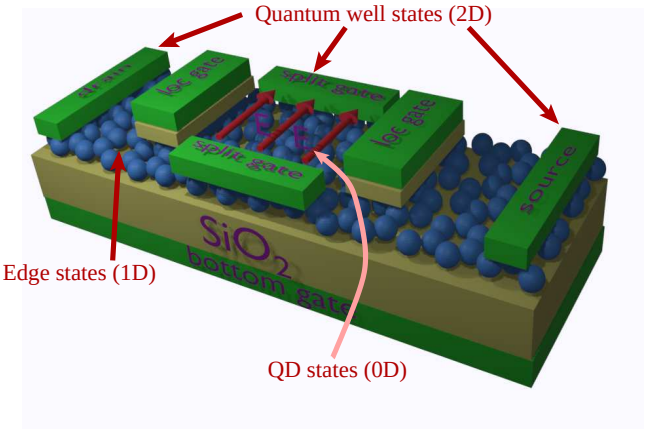

Fig. 1 The graphene laser setup with low-dimensional electron states in the quantum-dot (0D), nanoribbon (1D), and metal electrodes (2D).

entering Eq. (2) is defined for the thin metal electrodes representing the quantum-well layers embedding the quantum dots. The connection between the classical optical properties and the quantum mechanical formulation is given by

$$P(t) = \sum_{\alpha,\beta} \mu^*_{\alpha\beta} p_{\alpha\beta}(t)\,, \tag{3}$$

thereby establishing the relationship between $P(t)$ and the microscopic polarization amplitude $p_{\alpha\beta}$. In Eq. (3), α and β are the electron and hole states of the dots. We neglect the quantum-well transitions that are typically detuned from the laser field.

The microscopic polarization amplitude $p_{\alpha\beta}$ is obtained by solving the quantum mechanical semiconductor Bloch equations. For an active laser structure, these equations are derived using a Hamiltonian for the combined system of graphene quantum dots and thin metal electrodes, which represent the quantum wells [2]. We use the Maxwell–Bloch equations obtained in the screened Hartree–Fock limit [1]. They describe the time evolution of the microscopic polarization $p_{\alpha\beta}(t)$, and the level populations of electrons $n_{e\alpha}(t)$ and holes $n_{h\alpha}(t)$

$$\frac{dp_{\alpha\beta}}{dt} = -i\omega_{\alpha\beta_n} p_{\alpha\beta} - i\Omega^{\mathrm{R}}_{\alpha\beta_n}\left[n_{e\alpha} + n_{h\beta} - 1\right] + \frac{\partial p_{\alpha\beta}}{\partial t}\,|_{\mathrm{col}}\,, \tag{4}$$

$$\frac{dn_{e\alpha}}{dt} = \left[ip^*_{\alpha\beta}\Omega^{\mathrm{R}}_{\alpha\beta} + c.c.\right] - \gamma^d_{\mathrm{nr}} n_{e\alpha_n} + \frac{\partial n_{e\alpha}}{\partial t}\,|_{\mathrm{col}}\,, \tag{5}$$

$$\frac{dn_{h\beta}}{dt} = \left[ip_{\alpha\beta}\Omega^{\mathrm{R}}_{\alpha_n\beta} + c.c.\right] - \gamma^d_{\mathrm{nr}} n_{h\beta} + \frac{\partial n_{h\beta}}{\partial t}\,|_{\mathrm{col}}\,. \tag{6}$$

In Eqs. (4)–(6), the nonradiative and spontaneous emission carrier loss processes are approximated by the effective rate γ^d_{nr}. The terms $\partial/\partial t\,|_{\mathrm{col}}$ represent the collision contributions that are explained below. The details of derivations may be found in textbooks [1]. In Eqs. (4)–(6), we take into account the contributions from many-body

interactions via a renormalized transition energy $\hbar\omega_{\alpha\beta}$, the renormalization of the Rabi energy $\Omega^{\mathrm{R}}_{\alpha_n\beta}$ due to the screened Hartree–Fock contributions, and the many-body interaction giving rise to collisions causing dephasing of the polarization and relaxation of the population distributions $n_{e\alpha}$ and $n_{h\beta}$. In this approximation, we use microscopic relaxation rates in the screened Hartree–Fock equations instead of solving the full microscopic equations. Because the relaxation rates are computed independently of the integration of dynamic equations, this allows a considerable reduction in numerical demands. Contrary to the conventional effective rate treatment [3], the benefit of this approach is that it adequately describes scattering effects under lasing conditions.

Let us briefly discuss how the microscopic rate approximation is related to the full microscopic description, whose features are incorporated phenomenologically into our GL model. One example is polarization dephasing by collisions, whose quantum kinetic treatment, besides diagonal, also includes nondiagonal terms in $\partial p_{\alpha\beta}/\partial t\ |_{\mathrm{col}}$. In the lasers, the nondiagonal contribution is important for correctly describing the lineshape of gain and absorption spectra over a wide frequency range, and hence it cannot be neglected. Therefore, we account for both contributions appropriately. In the lasing conditions, when the lasing frequency is close to the gain peak and the intracavity carrier density is close to the threshold value, one can approximate the combined effect of diagonal and nondiagonal dephasing by introducing a simple rate. Ideally, the respective rate is obtained as a best fit to the numerical result when computing absorption/gain spectra, including diagonal and nondiagonal dephasing. This allows us to approximate the polarization dephasing term in the quantum-dot laser model [2]

$$\frac{\partial p_{\alpha\beta}}{\partial t}\ |_{\mathrm{col}} = -\gamma p_{\alpha\beta}, \tag{7}$$

where γ is the effective dephasing rate [1]. The microscopic polarization amplitude is then determined by solving the quantum mechanical semiconductor Bloch equations.

The non-classical light source consists of GL emitting single photons. By coupling two or more different GLs, one obtains a far more efficient analog of the SPDC devices in quantum optics. They allow the generation of the signal and idler photons used in quantum sensing, quantum teleportation, or remote interqubit coupling. By utilizing the coupled GLs, one no longer needs the SPDC approach. In GEP on Fig. 1 of main text, a short rectangular voltage pulse $V_{\mathrm{bias}}(t)$ generates three electromagnetic beams with distinct frequencies as schematically depicted in Figs. 1, 2 of main text. One component is the THz beam (I_1) idler, while the second and third components are the identical signal beams ($\mathrm{S}_{1,2}$) with the same frequency in the optical (VL) region. The last two beams, $\mathrm{S}_{1,2}$, serve two different functions: the second beam S_1 participates in the immediate THz sensing process, as explained below, while the third beam S_2 acts as the etalon signal directed straight to the output. Graphene quantum dots are promising candidates for on-demand generation of single photons and entangled photon pairs in various applications. However, their brightness becomes minimal due to total internal reflection at the interfaces. One way to overcome this limitation is to use a dielectric antenna structure [4]. With the antennas [4, 5], the photon extraction in GL is strongly increased in a broad spectral range.

Below, we briefly discuss the carrier capture and relaxation dynamics. We use a common reference for all the energies and chemical potentials, that is, the bottom of the quantum well. For the relaxation of a nonequilibrium carrier distribution, we study the relaxation of a nonequilibrium electron distribution generated by a pump pulse that matches a bulk state transition in our system. Immediately after the pump pulse, the electron populations in the quantum-dot, quantum-well, and bulk states, respectively, are driven by collisions toward distributions described by Fermi-Dirac functions$f\left(\varepsilon,\mu,T\right)=1/(\exp\left((\varepsilon-\mu)/(k_BT)\right)+1)$ where ε is the energy of the state, μ is the electrochemical potential, k_B is Boltzmann's constant and T is the temperature. The relaxation occurs on several characteristic time scales.

1) The fastest processe are scarrier–carrier collisions that involve continuous states in the quantum-well regions, i.e., in two (superscript 2) of the two subsystems (well, dot). These collisions drive the respective populations to quasi-equilibrium, so that

$$\{n_{e,\alpha},n_{e,\mathbf{k}_\perp}\}\rightarrow\{n_{e,\alpha},f\left(\varepsilon_{e,\mathbf{k}_\perp},\mu_e^{(2p)},T_{2p}\right)\},\tag{8}$$

where the label $2p$ marks the properties that are associated with the plasma (p) in the quantum-well regions. Below we discuss how $\mu_e^{(2p)}$ and T_{2p} are determined.

2) On the slowest time scale, the carrier–phonon collisions relax the quasi-equilibrium distributions in the quantum-well region from the temperature T_{2p} to the lattice temperature T_l

$$\{n_{e,\alpha},f\left(\varepsilon_{e,\mathbf{k}_\perp},\mu_e^{(2p)},T_{2p}\right)\}\rightarrow\{n_{e,\alpha_n},f\left(\varepsilon_{e,\mathbf{k}_\perp},\mu_e^{(2l)},T_l\right)\},\tag{9}$$

where we introduce an auxiliary electrochemical potential $\mu_e^{(2l)}$ for the quasi-equilibrium distributions, because of the temperature change.

Using the above phenomenological description of electron relaxation in the quantum-dot laser structure, and assuming that the process is similar for the hole populations, for the occupation in the quantum-dot states we have

$$\begin{aligned}\frac{\partial n_{\sigma,\alpha}}{\partial t}\mid_{\,\mathrm{col}}&=-\gamma_{\mathrm{c-c}}^{(2)}\left[n_{\sigma,\alpha}-f\left(\varepsilon_{\sigma,\alpha},\mu_\sigma^{(2p)},T_{2p}\right)\right]\\&\quad-\gamma_{\mathrm{c-p}}^{(2)}\left[n_{\sigma,\alpha}-f\left(\varepsilon_{\sigma,\alpha},\mu_\sigma^{(2l)},T_l\right)\right]-\gamma_{\mathrm{nr}}n_{\sigma,\alpha},\end{aligned}\tag{10}$$

where $\gamma_{\mathrm{c-c}}^{(2)}$ and $\gamma_{\mathrm{c-p}}^{(2)}$ are the effective relaxation rates for the entire (dot and well) carrier population by carrier–carrier and carrier–phonon collisions, respectively. Besides, we include a nonradiative loss term with an effective rate of γ_{nr}. Likewise, the equation of motion for the quantum-well populations is

$$\frac{\partial n_{\sigma,\mathbf{k}_\perp}}{\partial t}=-\gamma_{\mathrm{c-c}}^{(2)}\left[n_{\sigma\mathbf{k}_\perp}-f\left(\varepsilon_{\sigma\mathbf{k}_\perp},\mu_\sigma^{(2p)},T_{2p}\right)\right]-\gamma_{\mathrm{c-p}}^{(2)}\left[n_{\sigma\mathbf{k}_\perp}-f\left(\varepsilon_{\sigma\mathbf{k}_\perp},\mu_\sigma^{(2l)},T_l\right)\right],\tag{11}$$

where $\gamma_{\mathrm{c-c}}^{(2)}$ is the effective rate for the relaxation of the quantum-well populations due to carrier–carrier and carrier–phonon collisions, respectively, $\gamma_{\mathrm{nr}}^{\mathrm{qw}}$ and $\gamma_{\mathrm{nr}}^{\mathrm{b}}$ are the effective nonradiative carrier loss rates.

Above, we introduced the pump contribution as

$$\Lambda_{\sigma\mathbf{k}} = \frac{J\left(t\right)}{eh_b N_{p\sigma}} f\left(\varepsilon_{\sigma\mathbf{k}}, \mu_\sigma^p, T_l\right)\left(1 - n_{\sigma\mathbf{k}}\right), \tag{12}$$

where J is the injected current density when the pump pulse is applied, $f\left(\varepsilon_{\sigma\mathbf{k}}, \mu_\sigma^p, T_l\right)$, h_b, and $N_{p\sigma}$ are the steady-state electron or hole population and density in the absence of the laser field, and the factor $\left(1 - n_{\sigma\mathbf{k}}\right)$ accounts for blocking the pump due to the exclusion principle. The bias pulse $V_b\left(t\right)$ shifts the electron energy ε_α in the dot.

Solving the Maxwell–Bloch equations (4)–(6) with the relaxation contributions given by (11)–(12) requires knowing the Fermi–Dirac distributions at each time step. Let discuss how it is determined. When only the quantum-well and bulk populations are in quasi-equilibrium, the corresponding Fermi–Dirac distributions are obtained from the conditions

$$N_\sigma^q + N_\sigma^b = \frac{n_{\mathrm{qw}}}{A}\sum_{\mathbf{k}_\perp} f\left(\varepsilon_{\sigma\mathbf{k}_\perp}, \mu_\sigma^{(2p)}, T_{2p}\right) + \frac{h_b}{V_b}\sum_{\mathbf{k}} f\left(\varepsilon_{\sigma\mathbf{k}}, \mu_\sigma^{(2p)}, T_{2p}\right), \tag{13}$$

$$\begin{aligned} &\frac{n_{\mathrm{qw}}}{A}\sum_{\mathbf{k}_\perp}\varepsilon_{\sigma\mathbf{k}_\perp} n_{\sigma,\mathbf{k}_\perp} + \frac{h_b}{V_b}\sum_{\mathbf{k}}\varepsilon_{\sigma\mathbf{k}} n_{\sigma\mathbf{k}} \\ &= \frac{n_{\mathrm{qw}}}{A}\sum_{\mathbf{k}_\perp}\varepsilon_{\sigma\mathbf{k}_\perp} f\left(\varepsilon_{\sigma\mathbf{k}_\perp}, \mu_\sigma^{(2p)}, T_{2p}\right) + \frac{h_b}{V_b}\sum_{\mathbf{k}}\varepsilon_{\sigma\mathbf{k}} f\left(\varepsilon_{\sigma\mathbf{k}}, \mu_\sigma^{(2p)}, T_{2p}\right), \end{aligned} \tag{14}$$

and

$$N_\sigma^q + N_\sigma^b = \frac{n_{\mathrm{qw}}}{A}\sum_{\mathbf{k}_\perp} f\left(\varepsilon_{\sigma\mathbf{k}_\perp}, \mu_\sigma^{(2l)}, T_l\right) + \frac{h_b}{V_b}\sum_{\mathbf{k}} f\left(\varepsilon_{\sigma\mathbf{k}}, \mu_\sigma^{(2l)}, T_l\right). \tag{15}$$

We empasize that the transport of carriers between the different regions is considered as an integral part of the capture and relaxation processes due to carrier–carrier and carrier–phonon collisions.

In the numerical calculations, Eqs. (13) and (14) are solved for $\mu_\sigma^{(2p)}$ and T_{2p}, and (15) yields $\mu_\sigma^{(2l)}$. The label p indicate that the properties are associated with the plasma in the quantum-well and quantum dot regions while l marks the lattice properties. All the summations in these equations are performed numerically. We use the gauge to verify that the summations are performed to the necessary accuracy is to examine the extent to which total (matter and radiation field) energy is conserved. The results are shown in Fig. 3 of main text. From Fig. 3 of main text one can see that the time dependencies of $\mu^{(2l)}$, $\mu^{(2p)}$ and T_{2p} are expressed as four solutions (A-D) of the nonlinear equations (13)–(15). The solutions (A-D) correspond to four different nonequilibrium states inside GQD.

Below, we require that the radiation field energy change due to stimulated emission equals the energy change associated with changes in electron and hole populations, with a deviation less than 2%. This assumes that the solution of Eq. (15) is accurate. The adequacy of these calculations to the microscopic theory is observed under the following conditions. (*i*) The deviations from quasi-equilibrium are not too large. (*ii*) The effective relaxation times differ from each other, ensuring that the relaxation behavior demonstrates distinct properties of the different stages described earlier. That is not always the case for the collisions involving discrete states, the effective rates $\gamma^{(2)}_{\mathrm{c-c}}$ and $\gamma^{(2)}_{\mathrm{c-p}}$ can be over an order of magnitude slower than $\gamma^{(2)}_{\mathrm{c-c}}$ and $\gamma^{(2)}_{\mathrm{c-p}}$ [6, 7].

The effective relaxation rates used in our simulations are introduced as follows. For the quantum-well regions, the rates $\gamma^{(2)}_{\mathrm{c-c}}$ and $\gamma^{(2)}_{\mathrm{c-p}}$ are selected to fit the model to the microscopically calculated relaxation of the disturbed system back to a Fermi–Dirac distribution. Although there is a good overall agreement during the relaxation process, there are slight deviations of the shape of the spectral bump or hole. The deviations, however, only partially influence the nonequilibrium gain under the respective conditions. Typical room temperature effective relaxation rates for metal plates extracted from microscopic calculations are approximately 1 to 2×10^{13} s^{-1} for carrier–carrier collisions, and approximately 0.2 to 1×10^{12} s^{-1} for carrier–phonon collisions [14].

However, a similar comparison between approximate and microscopic treatments for a quantum-dot structure is not accurate because of a lack of a reliable numerical analysis of a complete microscopic model for the inhomogeneously broadened graphene quantum-dot structure shown in Fig. 1 of main text. Without such a comparison, the effective relaxation rates $\gamma^{(2)}_{\mathrm{c-c}}$ and $\gamma^{(2)}_{\mathrm{c-p}}$ are obtained by using the real parts of the scattering coefficients in the second Born approximation for carrier–carrier and carrier–phonon collisions, respectively. Currently, there is uncertainty concerning these values within the range 10^{10} s^{-1} to 10^{9} s^{-1} at room temperature.

2 The maximum conversion efficiency of graphene quantum dot laser

Let us evaluate the maximum conversion efficiency η_{GL} of GL. It is well known that SL [9–11] emitting conventional photons achieve over 30% peak ex-facet electrical-to-optical power conversion efficiency η_{Z} and stable far-field output with 75% coupling efficiency to PM fiber in a butterfly package. In the case of GL, emitting the single THz and optical photons, the generated power might be lower. To evaluate the the conversion efficiency, η_{Z}, of GL in generating the entangled idle and signal photons, we adopt an analytical model that depends on the output power level $\mathcal{P}$, pump pulse duration t_{pulse}, and the cavity length l [12, 13]. The applicability of the mentioned optimization scheme was discussed earlier [12, 13] to consider high-power diode lasers based on sub-monolayer InAs/GaAs quantum dots (QDs). Our aim here is to establish the dependence between the internal characteristics of GL and their efficiency.

Power conversion efficiency η_Z is defined as the ratio of the output optical power $\mathcal{P}$ from diode facets to the electrical input

$$\eta_Z\left(\mathcal{P},l\right)=\frac{\mathcal{P}}{I}\frac{1}{V_{t-o}+IR_{s-r}}, \tag{16}$$

where the drive current is $I=\mathcal{P}/\eta+I_{th}$ is applied to achieve the output power $\mathcal{P}$. The threshold current I_{th} depends on the cavity length l, on the differential efficiency η, the diode turn-on voltage is V_{t-o}, and on the series resistance of GL, R_{s-r}. Following Refs. [12, 13], to find the optimum diode length $l_{\rm opt}$ we use the condition $\partial\eta_Z(\mathcal{P},l)/\partial l\ |_{\mathcal{P}=\rm const}=0$. For the given power $\mathcal{P}$, the solution of the last equation defines the maximum $\eta_Z^{\max}(\mathcal{P})$ of the conversion efficiency. The above matching condition [12, 13] is rewritten in the form

$$Z(2R_{s-r}+\frac{V_{t-o}}{I})+I\frac{dR_{s-r}}{dl}=0, \tag{17}$$

where we defined $Z\equiv dI/dl\ |_{\mathcal{P}=\rm const}$. The magnitude of Z depends on $\mathcal{P}$ and l. Basically, due to variations of I_{th} and η_Z with l, the behavior of Z is complex. However, it becomes simplified for the GL geometry by using model expressions for $l_{\rm opt}$ and $\eta_Z^{\max}(\mathcal{P})$. For GL, we use the linear dependence between threshold current density, j_{th}, and modal gain, ζ

$$\zeta=\theta\left(j_{th}-j_0\right). \tag{18}$$

Above we assumed that $\zeta<\zeta^{\rm sat}$, where $\zeta^{\rm sat}$ is the saturated gain, θ is the differential gain (with respect to current density), and j_0 is current density at the transparency. Then we get

$$Z=\frac{\mathcal{P}\alpha_i}{\eta_0 r}+w\left(\frac{\alpha_i}{r}+j_0\right), \tag{19}$$

where η_0 is the internal differential efficiency, α_i is the internal loss, $r=(1/2)\ln(1/R_1R_2)$, $R_{1,2}$ are the facet power reflectivities. One receives expressions for the optimum GL cavity length, $l_{\rm opt}$, and for the maximum conversion efficiency, $\eta_Z^{\max}(\mathcal{P})$ by substituting Eq. (19) into (18). One gets

$$l_{\rm opt}=\frac{I_{\mathcal{P}}^0}{Z\sqrt{1+Q^2}},\qquad \eta_Z^{\max}(\mathcal{P})=\frac{\mathcal{P}}{V_{t-o}I_{\mathcal{P}}^0}\frac{Q}{\left(1+\sqrt{1+Q}\right)^2}, \tag{20}$$

where $Q=wV_{t-o}/\rho_s Z$ and $I_{\mathcal{P}}^0=\mathcal{P}/\eta_0+wr/\beta$ are length-independent parameters. The actual experimental GQD setup, like proposed in Fig. 1A of main text, is designed if the real device parameters are available. Unfortunately, there is a shortage of experiments on GL yet. Up to date, we can use projected parameters extracted from our earlier experimental works on the carbon nanotube quantum dot devices [4, 15, 22].

The estimated cavity length and facet reflectivities are used to evaluate the performance of the entangled photon generators like those sketched in Figs. 1, 2 of main text. On the one hand, by substituting the actual experimental parameters of the GQD laser, such as specific resistance and internal loss, one can facilitate the maximum conversion efficiency for the practically desired level of power output. On the other hand,

Eq. (20) allowed optimizing the laser structure for high-efficiency operation by estimating the relative importance of different internal parameters. For estimations we use the internal differential efficiency as $\eta_0 = 1.31$ W/A, $\rho_s = 1.244\times10^{-4}\Omega\cdot$ cm^2, and the differential gain for current density $\beta = 0.06$ cm/A. To estimate the one-photon output optical power from diode facets (the GL generated power) with the pulse duration $t_{\rm pulse} = 3.5$ ps we use the following parameters. For the one idle photon we take $\mathcal{P}_i = hf_i/t_{\rm pulse}$=0.33 nW, $V^{(i)}_{\rm bias} = hf_i/e = 4$ mV, $I_i = \mathcal{P}_i/V^{(i)}_{\rm bias} = 82$ nA. Then, in the case of interest $Z \to 0$, for the iddle GL one finds $l^{(i)}_{\rm opt} = 2.6$ mm, $I^{(i),0}_{\mathcal{P}} = 2.5$ μA, $\eta^{(i)\,\max}_{Z\to0} \simeq 0.07$. Besides, for the signal GL we use $V_{t-o} = V^{(s)}_{\rm bias} = 2.7$ V, $\mathcal{P}_s$=0.2 μW, $I_s = 80$ nA that gives $l^{(s)}_{\rm opt} = 4$ μm, $I^0_{\mathcal{P}} = 2.6$ μA, $\eta^{(s)\,\max}_{Z\to0} \simeq 0.03$.

On the one hand, the energy of solitary i- and s-photons generated by GL is lower than the energy of multiple photons generated by conventional semiconducting quantum dot lasers (SL) [9]. Respectively, the maximum conversion efficiency $\eta_{\rm GL}$ of GL is always lower than $\eta_{\rm SL}$ of SL [9]. Namely, for an idle THz photon, $\eta^{(i)}_{\rm GL}$ is estimated as $\sim 7\%$, while for an signal optical photon $\eta^{(s)}_{\rm GL} \simeq 3\%$. Thus, in either case, the estimated $\eta^{(i,s)}_{\rm GL}$ is lower than $\eta_{\rm SL} \sim 50\%$ reported in Ref. [9]. On the other hand, the GL generation is $\sim 10^4$ times more efficient than the traditional SPDC method, whose efficiency is typically below 4×10^{-6}.

3 Efficient generation of entangled photons with the graphene quantum dot lasers

Let us outline the microscopic mechanism of sensing with undetected THz photons. Up to now, for this purpose, one frequently uses spontaneous parametric down-conversion (SPDC), which is also referred to as parametric fluorescence or parametric scattering [18–21]. SPDC is a nonlinear, instantaneous optical process that converts a photon of higher energy (namely, a pump photon) into a pair of photons (namely, signal and idler photons) of lower energy, in accordance with the principles of energy conservation and momentum conservation. The total energy of the signal and the idler photons is equal to the energy of the pump photon. A recognized shortcoming of this approach is that the conversion efficiency of SPDC is rather low, not exceeding 4×10^{-6} of incoming photons for periodically poled lithium niobate (PPLN) in waveguides. Thus, when using the weak idle and signal beams, observing the "induced coherence without induced emission" is difficult. Besides, it requires a careful and complex tuning of the experimental setup. To improve the efficiency of the entangled photon generation process, we suggest replacing the SPDC-based method with a device involving graphene quantum dot lasers (GL) that have demonstrated remarkable perspectives in terms of efficiency, compact size, and flexibility [9–11].

We assume that a short rectangular pump pulse $V^{i,s}_{\rm bias}(t)$ excites simultaneously two GL$_{i1}$ and GL$_{s1}$ (here i and s stand for idle and signal respectively), as depicted in Figs. 1, 2 of main text. The third GL$_{s2}$ is excited independently and serves to generate an ethalon optical signal S$_2$ of the same frequency as S$_1$, and is used just to retrieve the signatures of the test sample. Let us first discuss the wave interaction in the active regions of GL$_{i1}$ and GL$_{s1}$. When the pump pulse harmonics $E_{p,l}\,(\mathbf{r},t)$

match the quantized level spacing $\Delta_{i,s}$ in the active regions of $\mathrm{GL}_{i,s}$, the respective $\mathrm{GL}_{i,s}$ generate the coherent electromagnetic waves $\hat{E}_{i,m}^{(-)}(\mathbf{r},t)$ and $\hat{E}_{s,q}^{(-)}(\mathbf{r},t)$, where indices l,m,q label three mutually orthogonal directions in space, while the indices p, i, and s stand for the pulse, idle, and signal respectively. The coupling between the three waves, $E_{p,l}(\mathbf{r},t)$, $\hat{E}_{i,m}^{(-)}(\mathbf{r},t)$ and $\hat{E}_{s,q}^{(-)}(\mathbf{r},t)$ occurs as follows. For instance, after the pump pulse $V_{\mathrm{bias}}^{i}(t)$ generates the laser emission in GL_i, the excited coherent wave $\hat{E}_{i,m}^{(-)}(\mathbf{r},t)$ causes a feedback influence $\beta_i(t)\hat{E}_{i,m}^{(-)}(\mathbf{r},t)$ on the pump signal itself, where $\beta_i(t)$ is obtained from the solution of the Maxwell–Bloch equations. Thus, the feedback influence modifies the initial pulse form of $V_{\mathrm{bias}}^{i,s}(t)$. This already modified pulse $\tilde{V}_{\mathrm{bias}}^{i,s}(t)$ acts on the other GL_s, thereby transferring the quantum state information from GL_i to GL_s. Accordingly, the same interaction mechanism takes place to transfer the quantum information from GL_s to GL_i. Although the waves $\hat{E}_{i,m}^{(-)}(\mathbf{r},t)$ and $\hat{E}_{s,q}^{(-)}(\mathbf{r},t)$ do not interact with each other directly, the significant interaction arises in the course the generation process of the idle and signal beams. The Hamiltonian is expressed [18–21] in the interaction picture as

$$\hat{H}_{int}(t)=\int_{D} d^{3}r\tilde{\kappa}_{lmq}E_{p,l}(\mathbf{r},t)\,\hat{E}_{i,q}^{(-)}(\mathbf{r},t)\,\hat{E}_{s,m}^{(-)}(\mathbf{r},t)+h.c., \tag{21}$$

where $\tilde{\kappa}$ is evaluated from the solution of the Maxwell–Bloch equations (4)–(6) and describes an effective coupling between the electric fields, $\hat{\mathbf{E}}_{s}^{(-)}(\mathbf{r},t)$ and $\hat{\mathbf{E}}_{i}^{(-)}(\mathbf{r},t)$ are the negative frequency parts of the quantized electric fields associated with the signal and idler, respectively, D is the volume of the GL active region, h.c. implies Hermitian conjugation, and there is summation over the repeated indices l,m,q. The active area of GL refers to the region where light amplification occurs, primarily due to stimulated emission from GL. The quantum dot confines electrons and holes in all three spatial dimensions, leading to unique electronic and optical properties. The active region is constructed to maximize the interaction between GL and the optical mode, enabling its operation.

The pump, the signal and the idler fields oscillate at different frequencies. In general, the GL generation efficiency depends on these frequencies. The Hamiltonian in Eq. (21) is therefore often expressed by decomposing the electromagnetic fields into several modes. The positive frequency part of a quantized electric field inside GL can be represented by the expression

$$\hat{\mathbf{E}}^{(+)}(\mathbf{r},t)=\sum_{\mathbf{k},\sigma}\alpha(\mathbf{k},\sigma)\exp\left[i\left(\mathbf{k}\cdot\mathbf{r}-\omega t\right)\right]e_{\mathbf{k},\sigma}\hat{a}(\mathbf{k},\sigma), \tag{22}$$

where $\sigma=1,2$, labels two directions of polarization, ω is the frequency, $\mathbf{k}$ is the wave vector, $\mathbf{e}_{\mathbf{k},\sigma}$ represents two generally complex, mutually orthogonal unit vectors such that $\mathbf{e}_{\mathbf{k},\sigma}\cdot\mathbf{k}=0$, $\alpha(\mathbf{k},\sigma)=i\sqrt{\hbar\omega/\left(2\epsilon_0 n^2(\mathbf{k},\sigma)L^3\right)}$, ϵ_0 is the electric permittivity of free space, $n(\mathbf{k},\sigma)$ is the refractive index of the anisotropic, nonlinear GL, L^3 is the quantization volume, and $\hat{a}(\mathbf{k},\sigma)$ is the photon annihilation operator for the mode labeled by $(\mathbf{k},\sigma)$. Let us also decompose the pump field inside GL into plane wave

modes and express it in the form

$$\mathbf{E}_p(\mathbf{r},t)=\sum_{\mathbf{k}_p,\sigma_p} V_p(\mathbf{k}_p,\sigma_p)\exp\left[i\left(\mathbf{k}_p\cdot\mathbf{r}-\omega_p t\right)\right]e_{\mathbf{k}_p,\sigma_p}. \tag{23}$$

The Equations (21)–(23) are written in general forms. For the sake of simplicity, we use assumptions that are appropriate to our GEP device. First, we assume that the signal and the idler can be treated as beams with uniform linear polarization both inside and outside of GL. Then, we drop the summation over the polarization indices σ_{p_j} , σ_{s_j}, σ_{i_j} and use

$$\alpha\left(\mathbf{k}_{s_j},\sigma_{s_j}\right)\approx\alpha\left(\omega_{s_j}\right),\quad \alpha\left(\mathbf{k}_{i_j},\sigma_{i_j}\right)\approx\alpha\left(\omega_{i_j}\right), \tag{24}$$

One can now replace the annihilation operator $\hat{a}(\mathbf{k},\sigma)$ with $\hat{a}(\mathbf{k})$, the number state $|\mathbf{k},\sigma\rangle$ with $|\mathbf{k}\rangle$ and the effective coupling between the electric fields $\tilde{\kappa}_{lmq}$ with a scalar quantity $\tilde{\kappa}$. The quantum state of light generated by GL is given by

$$|\psi(t')\rangle=|vac\rangle+\left[\frac{1}{i\hbar}\int_0^{t'}dt\hat{H}_{int}(t)\right]|vac\rangle+\ldots \tag{25}$$

where $|vac\rangle$ is the vacuum state and t' is the interaction time.

We assume that the graphene quantum dot lasers GL_{i1} (THz idle), GL_{s1} (optical signal), and GL_{s2} (ethalon optical signal) are pumped by the same rectangular beam P_1. The THz idler beam, I_1, generated by GL_{i1} is transmitted through the scan matrix and enters the test sample. Then I_1 is aligned with the idler beam, I_2, that is the output after passing the test sample. The optical signal beams S_1 and S_2 emmited respectively by GL_{s1} and GL_{s2} are also generated by the same pump pulse as the THz idler beam, I_1. The second beam S_2 will later serve as ethalon to retrive the test sample image. To mix the THz idle beam I_2 with the optical signal beams S_1 one uses the dichroic mirror DM_1. The combined beam I_2 + S_1 output of DM_1 is directed to separate it into modified signal beam S_1' and the idle beam I_1 that is disposed. In the next step, by using a beam-splitter, BS, the optical beam S_1' is superposed with the ethalon optical beam S_2 to retrieve the test sample information. One of the outputs of the beam splitter is detected by an EMCCD camera. Suppose that the pump fields at the two GLs are given by the complex electric field vectors $\mathbf{E}_{p_1}(\mathbf{r}_1,t_2)$ and $\mathbf{E}_{p_2}(\mathbf{r}_2,t_2)$, expanded in the form given by Eq. (23). From Eqs. (22), (23), (24) and (25) it follows that the quantum state of light generated by each individual GL is given by the formula (cf. [18–21])

$$\begin{aligned}|\psi_j(t')\rangle\;=\;&|vac\rangle+\frac{t'D}{i\hbar}\sum_{\mathbf{k}_{p_j}}\sum_{\mathbf{k}_{s_j}}\sum_{\mathbf{k}_{i_j}}\breve{\kappa}\left(\omega_{p_j},\omega_{s_j},\omega_{i_j}\right)\exp\left[i\left(\mathbf{k}_{p_j}-\mathbf{k}_{s_j}-\mathbf{k}_{i_j}\right)\cdot\mathbf{r}_{0_j}\right]\\&\times\operatorname{sinc}\left[\left(\omega_{s_j}+\omega_{i_j}-\omega_{p_j}\right)\frac{t'}{2}\right]\left\{\prod_{n=1}^{3}\operatorname{sinc}\left[\left(\mathbf{k}_{p_j}-\mathbf{k}_{s_j}-\mathbf{k}_{i_j}\right)_n\frac{l_n}{2}\right]\right\}\end{aligned}$$

$$\times \left|\mathbf{k}_{s_j}\right\rangle_{s_j} \left|\mathbf{k}_{i_j}\right\rangle_{i_j}] + \ldots \tag{26}$$

where $j = 1, 2$ labels the two GLs, $\breve{\kappa}\left(\omega_{p_j}, \omega_{s_j}, \omega_{i_j}\right) = V_{p_j}\left(\mathbf{k}_{p_j}\right) \cdot \alpha^*\left(\mathbf{k}_{s_j}\right) \alpha^*\left(\mathbf{k}_{i_j}\right) \exp\left[i\left(\omega_{s_j} + \omega_{i_j} - \omega_{p_j}\right) t'/2\right]$, $\left|\mathbf{k}_{s_j}\right\rangle_{s_j} = \hat{a}^\dagger_{s_j}\left(\mathbf{k}_{s_j}\right)|vac\rangle_{s_j}$, $\left|\mathbf{k}_{i_j}\right\rangle_{i_j} = \hat{a}^\dagger_{i_j}\left(\mathbf{k}_{i_j}\right)|vac\rangle_{i_j}$, and $\mathrm{sinc}[x] = \sin x/x \approx x$; the sinc terms lead to the two *phase matching conditions* associated with the process of GEP-generated entangled photons. We assume that the volume integration is carried out over the GL active region representing a rectangular parallelepiped of sides l_1, l_2, l_3 with its center located at the point r_{0_j}.

Except for the newly introduced wave interaction mechanism, the calculations below are similar to conventional SPDC-based theory [18–21]. We reproduce it just for convenience, keeping in mind that the laser-induced interwave coupling is considerably stronger than SPDC. If the beam I_1 is perfectly aligned with the beam I_2, for each mode present in the quantized field $\hat{E}^{(+)}_{I_1}(\mathbf{r}, t)$ of I_1 there exists an equally populated mode in the quantized field $\hat{E}^{(+)}_{I_2}(\mathbf{r}, t)$ of I_2. The condition of perfect alignment of the idler beams is

$$\hat{a}_{I_2}\left(\mathbf{k}_i\right) = \hat{a}_{I_1}\left(\tilde{\mathbf{k}}_i\right) \exp\left[i\phi_i\left(\tilde{\mathbf{k}}_i\right)\right] \tag{27}$$

where the mode $\tilde{\mathbf{k}}_i$ is the output of test sample and is aligned with the mode $\mathbf{k}_i$ that is generated at GL_{i1}; $\phi_i\left(\tilde{\mathbf{k}}_i\right)$ is a phase factor gained by the mode $\tilde{\mathbf{k}}_i$. When the diffraction limits are neglected, there is a full correspondence between $\mathbf{k}_i$ and $\tilde{\mathbf{k}}_i$.

The above classical formulation illustrates the quantum mechanical problem. The quantized field decomposes into several plane wave modes, assuming that one point on the test sample can transmit and reflect only one specific mode of the quantized idler field. Thus, a single point on the test sample acts as a beam splitter only on one particular idler mode. In terms of quantum mechanics, the alignment condition becomes

$$\hat{a}_{I_2}\left(\mathbf{k}_i\right) = \left[\mathcal{T}\left(\rho_{\tilde{\mathbf{k}}_i}\right) \hat{a}_{I_1}\left(\tilde{\mathbf{k}}_i\right) + \mathcal{R}'\left(\rho_{\tilde{\mathbf{k}}_i}\right) \hat{a}_0\left(\tilde{\mathbf{k}}_i\right)\right] \exp\left[i\phi_i\left(\tilde{\mathbf{k}}_i\right)\right] \tag{28}$$

where we introduced $\mathcal{T}\left(\rho_{\tilde{\mathbf{k}}_i}\right)$ as the transmission coefficient of the object at the point $\rho_{\tilde{\mathbf{k}}_i}$, $\mathcal{R}'\left(\rho_{\tilde{\mathbf{k}}_i}\right)$ is the reflection coefficient at the same point when illuminated from the opposite direction, $\hat{a}_0$ is the vacuum field at the point on the object, $\phi_i\left(\tilde{\mathbf{k}}_i\right)$ is the phase term, and there is the normalization condition $|\mathcal{T}|^2 + |\mathcal{R}'|^2 = 1$. When the object is absent ($\mathcal{T} = 1$ and $\mathcal{R}' = 0$), Eq. (27) and Eq. (28) coincide with each other.

When neglecting the diffraction, the positive frequency part of the quantized field at the camera can be expressed as

$$\hat{E}^{(+)}_s\left(\rho_{\mathbf{k}_s}, t\right) \propto \exp\left[-i\tilde{\omega}_s\left(t - \frac{L_1\left(\mathbf{k}_s\right)}{c}\right)\right] \hat{a}_{s_1}\left(\mathbf{k}_s\right), \tag{29}$$

where $L_j(\mathbf{k}_s)$ is the optical path traveled by the mode labeled by $\mathbf{k}_s$ from GL_j to the camera (propagation inside the GLs has been neglected), $|\mathbf{k}_s| = \bar{\omega}_s/c$.

For the sake of simplicity, we assume that the pump beams are well collimated, uniformly polarized, and narrow-band with mean frequency $\bar{\omega}_p$. In this case, the pump field at the GL_j can be represented by $V_{p_j}\exp[i(\mathbf{k}_p\cdot\mathbf{r}-\bar{\omega}_p t)]$. We choose the direction of $\mathbf{k}_p$ to be along the direction of the optical axis. We assume that GLs are with sides below 10^{-3} m of length; then we use that the wave vectors correspond to certain respective optical wavelengths. This means that the terms $\operatorname{sinc}\left[\left(\mathbf{k}_{p_j}-\mathbf{k}_{s_j}-\mathbf{k}_{i_j}\right)_n l_n/2\right]$ in Eq. (26) contribute only when $\mathbf{k}_{p_j}-\mathbf{k}_{s_j}-\mathbf{k}_{i_j}\approx 0$. The respective spatial phase matching condition $\mathbf{k}_{p_j}\approx\mathbf{k}_{s_j}+\mathbf{k}_{i_j}$ is fairly accurate. Moreover, the term $\operatorname{sinc}\left[\left(\omega_{s_j}+\omega_{i_j}-\bar{\omega}_p\right)t'/2\right]$ in Eq. (26) leads to the temporal phase matching condition $\bar{\omega}_p\approx\omega_{s_j}+\omega_{i_j}$.

The photon counting rate [21] at a point $\rho_{\mathbf{k}_S}$ in the camera is

$$\mathcal{R}(\rho_{\mathbf{k}_s})\propto\langle\Psi|\,\hat{E}_s^{(-)}(\rho_{\mathbf{k}_s},t)\,\hat{E}_s^{(+)}(\rho_{\mathbf{k}_s},t)\,|\Psi\rangle \tag{30}$$

where $|\Psi\rangle=|\psi_1(t')\rangle+|\psi_2(t')\rangle$ and the quantized field is given by Eq. (29). Apart from a proportionality constant one gets [18] the key equation of the theory of imaging

$$\begin{aligned}\mathcal{R}(\rho_{\mathbf{k}_s})\approx{}&|V_{p_1}|^2+|V_{p_2}|^2+2\,|V_{p_1}|\,|V_{p_2}|\left|\mathcal{T}\left(\rho_{\tilde{\mathbf{k}}_i}\right)\right|\\&\times\cos[\phi_{s_2}(\mathbf{k}_s)-\phi_{s_1}(\mathbf{k}_s)-\phi_i(\mathbf{k}_i)\\&-\arg\left[\mathcal{T}\left(\rho_{\tilde{\mathbf{k}}_i}\right)\right]+\phi_p+\mathbf{k}_s\cdot\mathbf{r}_0+C_0]\end{aligned} \tag{31}$$

where $\tilde{\mathbf{k}}_i$ denotes a wave vector that is the mirror image of the wave vector $\mathbf{k}_i=\mathbf{k}_p-\mathbf{k}_s$ with respect to the optical axis, $|\mathbf{k}_p|=\bar{\omega}_p/c$, $|\mathbf{k}_s|=\bar{\omega}_s/c$, $|\mathbf{k}_i|=\bar{\omega}_i/c$, $\rho_{\tilde{\mathbf{k}}_i}$ is the point on the object that is illuminated by the idler mode $\tilde{\mathbf{k}}_i$, $\phi_{s_j}(\mathbf{k}_s)=\bar{\omega}_s L_j(\mathbf{k}_s)/c$, $\phi_p=\arg[V_{p_2}]-\arg[V_{p_1}]$, and C_0 represents all other phase terms.

Using the above equations, one derives conditions for constructive and destructive interference. Furthermore, one can observe that the information of the object appears only in the interference term. This suggests that the imaging process is purely quantum mechanical.

References

[1] W. W. Chow and S. W. Koch, Semiconductor-Laser Fundamentals: Physics of the Gain Materials. Berlin, Germany: Springer-Verlag, 1999.

[2] W.W. Chow, H. C. Schneider, S.W. Koch, C. H. Chang, L. Chrostowski, and C. J. Chang-Hasnain, Nonequilibrium model for semiconductor laser modulation response, IEEE J. Quantum Electron., **38**, 4, 402 (2002).

[3] K. Y. Lau, Dynamics of quantum well lasers, in QuantumWell Lasers, P. S. Zory Jr., Ed. Boston, MA: Academic, 1993, ch. 5.

[4] J. Yang, C. Nawrath, R. Keil, R. Joos, X. Zhang, B. Höfer, Y. Chen, M. Zopf, M. Jetter, S. L. Portalupi, F. Ding, P. Michler, And O. G. Schmidt, Quantum dot-based broadband optical antenna for efficient extraction of single photons in the telecom O-band, Optics Express, **28**, 13, 19457 (2020) https://doi.org/10.1364/OE.395367

[5] G. Atmatzakis, C. G. Christodoulou, D. Murell and L. F. Lester, RF power extraction from a quantum dot mode locked laser connected to an antenna, Proceedings of the 2012 IEEE International Symposium on Antennas and Propagation, Chicago, IL, USA, 2012, pp. 1-2, doi: 10.1109/APS.2012.6349096.

[6] H. Benisty, C.M. Sotomayor-Torres, and C.Weisbuch, Intrinsic mechanism for the poor luminescence properties of quantum-box systems, Phys. Rev. B.,**44**, R10945 (1991).

[7] M. Sugawara, K. Mukai, and H. Shoji, Effect of phonon bottleneck on quantum-dot laser performance, Appl. Phys. Lett., **71**, 2791 (1997).

[8] S. Shafraniuk, Thermoelectricity and Heat Transport in Graphene and Other 2D Nanomaterials. Micro and Nano Technologies. 2017, Philadelphia, United States: Elsevier - Health Sciences Division. 546.

[9] M. Buyalo, A. Gubenko, S. Mikhrin, V. Mikhrin, A. R. Kovsh, A.V. Krishnamoorthy, Efficient, high-power, narrow-linewidth, continuous-wave quantum-dot semiconductor comb laser, Scientific Reports **14**, 4197 (2024) https://doi.org/10.1038/s41598-024-53609-9.

[10] I. Khanonkin, S. Bauer, V. Mikhelashvili, O. Eyal, M. Lorke, F. Jahnke, J. P. Reithmaier, G. Eisenstein, On the principle operation of tunneling injection quantum dot lasers, Progress in Quantum Electronics, **81**, 100362 (2022).

[11] F. Jahnke, S. Michael, M. Lorke, Ultrafast carrier dynamics in tunnel-injection quantum-dot lasers, Proc. PC11999, Ultrafast Phenomena and Nanophotonics XXVI; PC119990N (2022) https://doi.org/10.1117/12.2610679, SPIE OPTO, (2022).

[12] A. E. Zhukov, A. R. Kovsh, S. S. Mikhrin, et al, Power conversion efficiency in a quantum dot based diode laser, 8th Int. Symp. "Nanostructures: Physics and Technology" LOED.1Op, St Petersburg, Russia, June 19-23, 2000.

[13] D. P. Bour and A. Rosen, Optimum cavity length for high conversion efficiency quantum well diode lasers, J. Appl. Phys. **66** 2813 (1989).

[14] S. Shafranjuk, Graphene: Fundamentals, Devices, and Applications (Pan Stanford, New York, 2015).

[15] M. Rinzan, G. Jenkins, H. D. Drew, S. Shafraniuk, and P. Barbara, Carbon Nanotube Quantum Dots As Highly Sensitive Terahertz-Cooled Spectrometers. Nano Letters, 2012. 12(6): p. 3097-3100.

[16] S. E. Shafraniuk, Resonant transport through a carbon nanotube junction exposed to an ac field, Journal of Physics: Condensed Matter,11 (2011); DOI: 10.1088/0953-8984/23/49/495304.

[17] S. E. Shafraniuk, Electromagnetic properties of the graphene junctions, The European Physical Journal B, 3 (2011); DOI: 10.1140/epjb/e2011-10675-3.

[18] M. Lahiri, R. Lapkiewicz, G. B. Lemos, and A. Zeilinger, Theory of quantum imaging with undetected photons, Phys. Rev. A **92**, 013832 (2015).

[19] L. Mandel, "Coherence and indistinguishability", Opt. Lett. **16**, 1882 (1991).

[20] X. Y. Zou, L. J. Wang and L. Mandel, "Induced Coherence and Indistinguishability in Optical Interference," Phys. Rev. Lett. **67**, 318-321 (1991).

[21] L. J. Wang, X. Y. Zou and L. Mandel, "Induced Coherence without Induced Emission," Phys. Rev. A **44**, 4614-4622 (1991).

[22] S. Mayle, T. Gupta, S. Davis, V. Chandrasekhar, and S. Shafraniuk, Thermometry and thermal management of carbon nanotube circuits, J. of Appl. Phys. **117**, 194305 (2015).